Article Identifier
DOI: 10.22032/dbt.58684
URN: urn:nbn:de:gbv:ilm1-2023isc-034:0

60th ILMENAU SCIENTIFIC COLLOQUIUM
Technische Universität Ilmenau, 4 – 8 September 2023
URN: urn:nbn:de:gbv:ilm1-2023isc:1

Development of a test setup for the characterization of an optical microscope for high precision length metrology applications

R.Köning, E.Schoetka, D.Bergmann, J.Krüger, M.Janik, M.Schumann, B.Bodermann

Physikalisch-Technische Bundesanstalt (PTB), Bundesallee 100, 38116 Braunschweig, Germany

ABSTRACT

A test setup to qualify the performance of optical microscopes has been designed and optimized using FEM calculations to exhibit a minimal susceptibility to thermal and mechanical influences of the ambient environment. The alignment is performed using an alignment autocollimator and alignment targets. The data acquisition of the camera and the position sensors of the stage is synchronized. The short-term repeatability (1σ) of the line position and -width measurement obtained with the integrated UV microscope are 1 nm and 0.2 nm respectively. In long-term measurements the maximum lateral and focus drift rate observed were 30- and 20 nm / hour respectively. The measured point spread function contained only radial symmetric optical aberrations. Using the Zernike-Nijboer theory including only the defocus and spherical aberrations, fit residuals were obtained that contain systematic deviations in the order of the noise level.

Index Terms – Optical Microscopy, Optical Aberrations, Image Simulation, Mechanical Design, Data acquisition, Synchronization, Zernike-Nijboer theory

1. INTRODUCTION

The Nanometer Comparator [1] at PTB is the national standard for the calibration of line scales. Its main task is the calibration of line distances on line scales and photomasks with measurement uncertainties in the single digit nanometer regime. Here the optical microscope used to image and detect the position of the line structures has a dominant role so that much work has been devoted to further improvements of the line position detection. In addition, there is a strong demand for bidirectional measurements, such as linewidth and diameter, measurements. To be able to proceed with the aforementioned developments without disturbing the operation of the Nanometer Comparator a test setup for optical microscopes has been developed.

To provide meaningful results that allow to draw the conclusion whether a new measure or method may potentially lead to an improvement of the optical structure localization in measurements at the Nanometer Comparator, the test setup has to allow to achieve related results with a repeatability of a few nanometers only as well. At the same time, as resources and funding were limited, some intelligent solutions had to be found and some compromises to achieve the required performance.

We will describe the optics of a UV microscope considered here first, from which we derive the related requirements of the mechanical setup. The chosen solution will be described in the next section. Then we will discuss the data acquisition and evaluation scheme. Here larger efforts were taken to obtain a good synchronization of the acquisition of the image and position data. In order to demonstrate the performance of the UV microscope we describe the results of the characterization of stability of the measurement results and discuss the determination of its optical aberrations using measurements of the point spread function. In the last section we will summarize the results and provide an outlook on further improvements of the setup.

2. OPTICS OF THE UV-MICROSCOPE

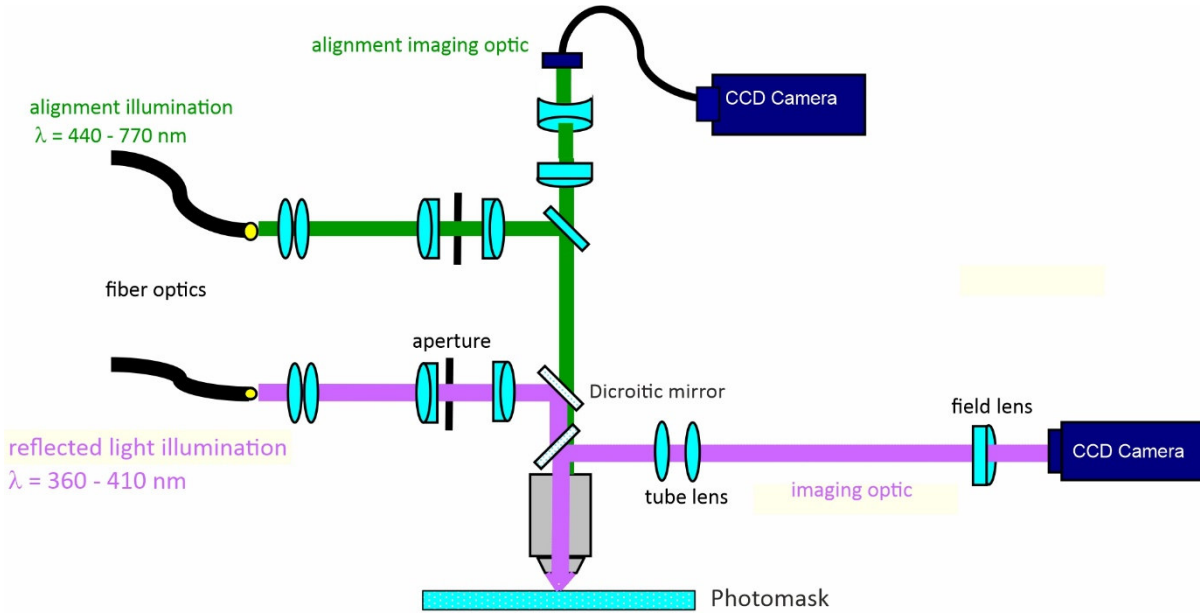

Figure 1: Optical layout of the UV microscope.

The microscope optics originates from a LMS IPRO 4 photomask metrology system of KLA Tencor [2] (formerly Vistec and Leica Microsystems, respectively). The optical layout is shown in Fig. 1. The original LMS IPRO microscope is additionally equipped with a transmitted light option and an autofocus sensor. The transmitted light modus would require introducing a large aperture into the measurement slide of the Nanometer Comparator, which would weaken its mechanical structure so that it would become very susceptible to mechanical vibrations. Therefore, any advantage gained from an improved contrast of the transmitted light mode would very likely not lead to an improved structure localization due to the higher level of mechanical vibrations expected. The stage used at the test setup also has only a limited aperture so that only a restricted area of the sample, usually a photomask, could be reached.

In both setups the height of the focal plane is determined during the alignment of the microscope and the sample can be aligned with respect to the focal plane using an optical probe. In addition, to eliminate any focus drift influences occurring over time, usually a series of images at different heights are taken from which the exact focus position is determined up in front of any investigation. Therefore, the autofocus sensor is not required. The microscope consists of two imaging and illumination branches. The tube lens in the UV imaging path is designed to provide a four times larger magnification than specified by the objective while the tube lens of the alignment does not introduce any additional magnification. In this way an overview microscope using the same objective is implemented. The use of an objective revolver can thus be avoided and related instabilities are eliminated. Using this lower magnification eases locating the desired objects on the sample and positioning them in the field of view of the UV camera considerably. The overview microscope is illuminated using green light. The light of the measurement and overview microscope are separated by a dichroitic mirror, which only reflects the UV light to the measurement camera.

2.1 Objectives

There are two different 50x objectives available with a numerical aperture of 0.55 and 0.9 and working distances of 6.8 mm and 0.3 mm. These objectives are based on the HCX PL APO U-V-I series of Leica and are still available from KLA Tencor in small numbers. These objectives are designed for a very broad spectral range from 350 nm to over 1000 nm. The objectives consist of cemented lens groups. They withstand UV radiation, but the damage threshold of the intensity is not known so that the use of a laser as light source is not advisable. Due to this high total magnification of 200 and the size of the chip of the measurement camera (6.5 mm x 4.8 mm) the field of view is limited to about 32 µm x 24 µm. Meanwhile, for the overview microscope, a camera with a larger chip (11.26 mm x 11.26 mm) is used resulting in field of view of about 225 µm x 225 µm.

2.2 Illumination

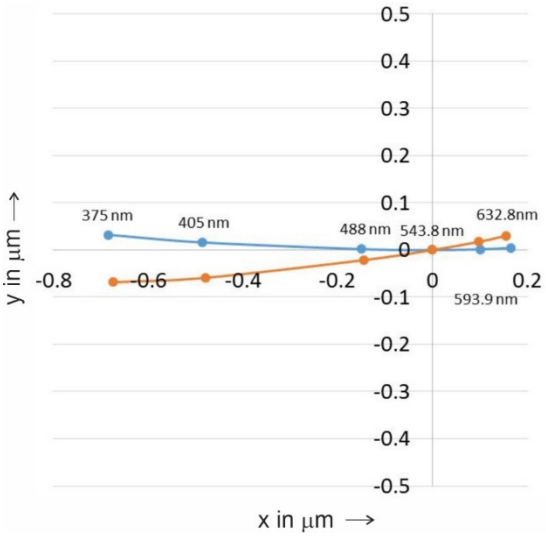

Figure 2: Wavelength dependence of the shift of a light spot for two objectives of the same type as used at the UV-microscope calculated from the wavelength dependence of the chromatic aberrations measured by the manufacturer.

2.2.1 Light source

The resolution of an optical microscope d_o is commonly related to

$$d_o = k_1 \frac{\lambda}{NA},$$

where k_1 is a system specific constant, which is in the order of 1, λ denotes the illumination wavelength and NA terms the numerical aperture of the objective. Therefore, both a shorter illumination wavelength and a higher NA lead to a higher resolution, which promises a lower uncertainty of the optical structure localization. However, there are some other aspects that need to be considered as well:

- The depth of field and the depth of focus decrease proportional to λ/NA^2. So, the smaller the wavelength and the higher the numerical aperture the more important are the focus control and the greater the influence of focus drift effects.
- If the wavelength gets smaller than 400 nm then the selection of additional optical elements such as fibers, lenses or polarizers then has to take the optical absorption into account.
- With decreasing wavelength and increasing photon energy the chance of depositing contaminations, which are always present in the environment, and on the surfaces of the microscope optics or the measurement objects, by photo induced chemical reactions is increasing.
- If the light source is a laser its spatial coherence has to be decreased by special methods to avoid speckle effects do not influencing the image quality. In addition, as already mentioned before, the intensity has to be kept below the damage threshold of the microscope optics (cement and coatings) and of the sample.
- The emission wavelength and the intensity need to be sufficiently stable. If an 8 bit Camera is used then the relative intensity noise (1σ) of the light source should be about 0.4% or smaller. Fig. 2 shows the wavelength dependence shift of the position of a light spot for two objective lenses (NA=0.55) of the same type used here. The shift was determined from the measurements of the chromatic aberrations measured by the manufacturer. The wavelength stability required to reach a position stability of 0.1 nm based on the measurements needs to be below 25 pm. In addition, image simulations including only the light matter interaction show that an uncorrected change of the wavelength of 2 nm leads to a deviation of linewidth of about 1 nm [3]. Similar

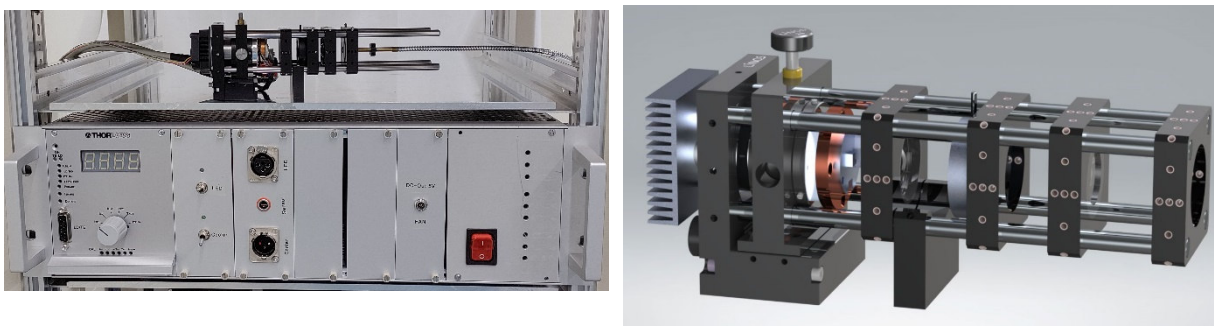

Figure 3: Left: Photo of the UV LED light source. Right: CAD model of UV-LED mount and the optics used to couple the light into a fiber.

deviations are to occur at other bidirectional measurement measurands, such a diameter of a circle.

In the original setup a high-pressure xenon mercury gas discharge lamp was used as light source of the UV microscope. However, a xenon light bulb has a limited lifetime of about 3000 hours. In addition, switching it on and off every day reduced the lifetime even further. Therefore, we replaced this lamp by a self-engineered, temperature-controlled UV LED source. It consists of a commercially available LED mounted on a thick aluminum circuit board [4] and a laser diode controller [4] capable to provide sufficient current for the control of the diode current and the temperature. using an additional thermoelectric cooler. Fig. 3 shows a photo and a CAD model of the LED and the optics used to couple the light into the fiber. Fig. 4 shows the drift of the intensity and the emission wavelength for a halogen lamp, a high pressure xenon mercury lamp and the aforementioned LED over a time frame of 40 hours. The LED shows a slight drift of 1.6 % peak to peak and exhibits the smallest standard deviations. In addition, the drift of the emission wavelength allows to reach a position stability of 0.1 nm.

There are no special requirements for the light source of the overview microscope. A halogen lamp worked well for several years. In the moment a LED light source is used.

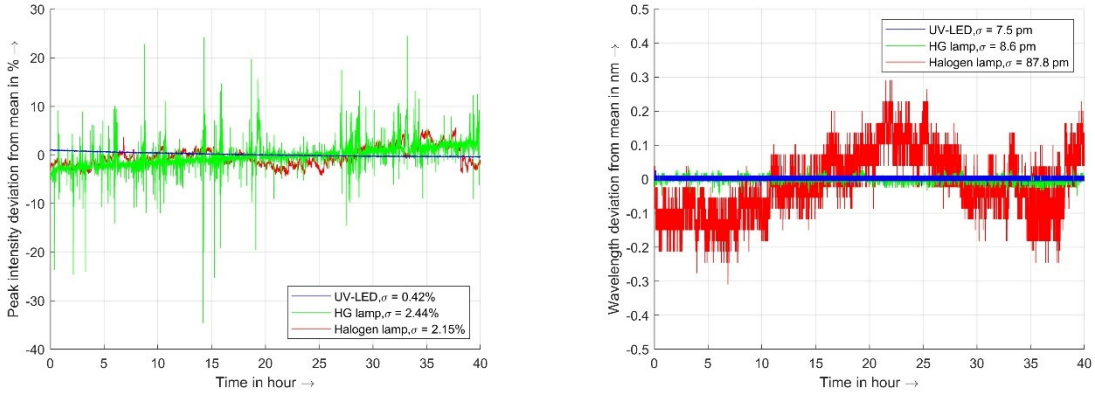

Figure 4: Left: Relative intensity noise in percent for different light sources. Right: Drift of the central emission wavelength

2.2.2 Illumination optics

To keep the dissipated power away from the setup the optical radiation is transferred by fibers to both imaging systems. Because the fiber of the overview microscope is not important, we restrict the discussion to the fiber of the measurement / UV microscope. This quartz glass fiber exhibits one core with 800 µm diameter and has a numerical aperture of 0.22. In the past we also used incoherent fiber bundles in the illumination path of the microscope at the Nanometer Comparator [1]. Unfortunately, the fiber ends were not located in the same plane, which prevented the realization of an exact Köhler illumination scheme, which is required to obtain a homogenous and well-defined illumination distribution. In addition, to the best of our knowledge, a Köhler illumination is perquisite for all program packages available to simulate optical images. These simulations are required to perform accurate

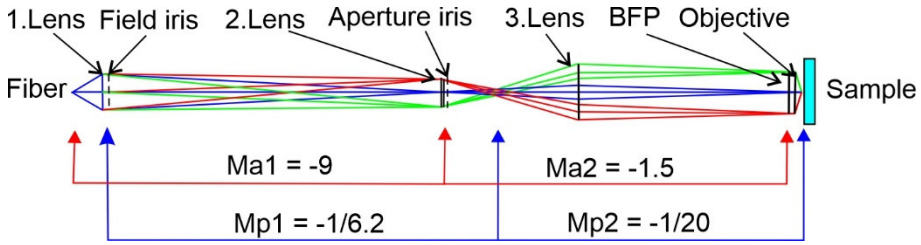

Figure 5: Illumination optics of the UV-microscope. Ma and Mp denote the magnification of the aperture and the pupil between the related conjugated planes whose position is indicated by the arrows. Note: dimensions are not to scale.

bidirectional optical measurements. Furthermore, to achieve a small defocus dependence of the measurement results the Köhler illumination scheme needs to be telecentric, that is, the effective illumination is not allowed to change when the distance between the measurement object and objective lens varies.

The schematic in the right part of Fig. 3 shows the optics used to couple the radiation into the fiber. It consists of two identical aspheric condenser lenses and an iris diaphragm. The LED light is collected and collimated by the 1st lens. The 2nd lens focusses the beam onto the fiber. The iris diaphragm is located between the two lenses in the parallel beam segment and allows to block that part of the radiation that is not accepted by the fiber due to its limited NA. We will add an additional electromechanical shutter here as well soon so that the contamination of the microscope optics and the sample due to UV radiation can be minimized. The position of the LED can be adjusted by a 3D stage to optimize the coupling of the intensity into the fiber.

The light emitted from the fiber needs to be imaged in the back focal plane (BFP) of the objective. A schematic of the optics used for this purpose is shown in Fig. 5. The 1st lens is located right behind the fiber and the 2nd in the mount of the aperture stop. The 3rd lens is mounted in the wall of the microscope housing / body (see Fig. 11). Note that the beam splitter and the dichroitic mirror, which are also located in the microscope housing, have been omitted here to reduce the complexity of the drawing. The beam diameter in the aperture planes (images of the fiber end, which acts as light source) needs to be magnified to fully fill the entrance pupil in the BFP of the objective and to enable the usage of high numerical aperture values of the illumination. The field diameter instead is considerably reduced to concentrate the light in the imaged region of the sample. Disadvantageous in this design is the location of both iris diaphragms very close to the lenses. It leads to difficulties in the realization of the required alignment normal to the optical axis.

2.3 Tube lens system of the UV imaging beam path

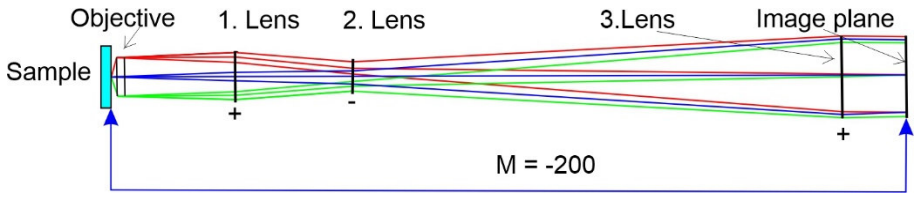

Figure 6: Schematic of the imaging path of the UV-microscope. Note: dimensions are not to scale.

The optical model of the imaging path is illustrated in Fig. 6. The tube lens system consists of 3 lenses. The 1st lens is mounted in the microscope housing, the 3rd lens in the camera adapter. While the 1st and 3rd lens exhibit a positive, the 2nd lens exhibits negative focal length. As already mentioned before, the tube lens system magnifies the image by an additional factor of four so that the total magnification of the UV-microscope becomes 200 when a 50x objective is used.

2.4 Camera

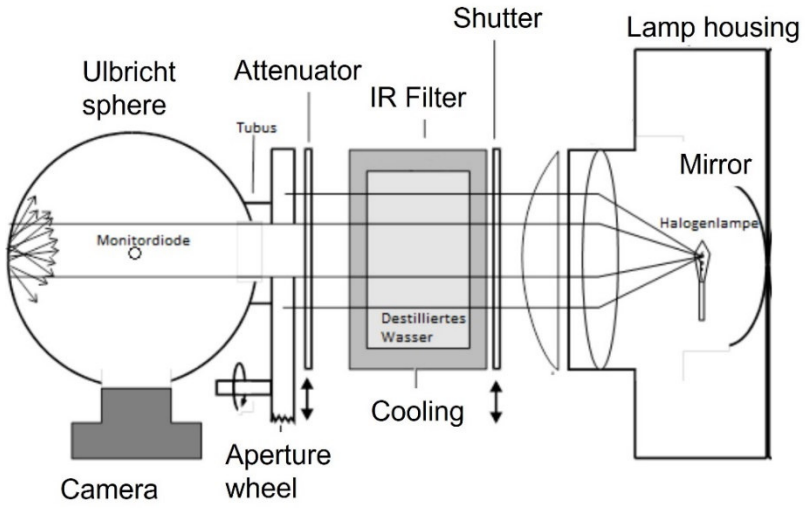

Figure 7: Schematic of the setup used to determine the nonlinear deviation of the camera. Note that the dimensions are not to scale. See [5] for further details.

The cameras are connected through the c-mount thread to the setup. Because the distance between the camera chip and the end of the housing varies for different cameras, adjustments may be required to move the surface of the chip in the nominal image plane when the camera is changed.

For the overview camera there are no special requirements but for a convenient alignment of the measurement object, the camera needs to be able to acquire at least 10 images / sec. In addition, a low power consumption is beneficial. Here an analog CCD camera with remote head was used for a long time. It was replaced by a network CMOS camera, which uses a larger chip so that the field of view could be extended as described section 2.1. However, for time consuming investigations or measurements the camera and light source of the overview microscope will be turned off and the setup will allow to thermalize overnight.

For the measurement camera the spectral sensitivity, the linearity of the intensity response, the noise, the effective pixel size, the deviation of the pixel from the nominal position in the matrix on the chip and the power consumption need to be considered.

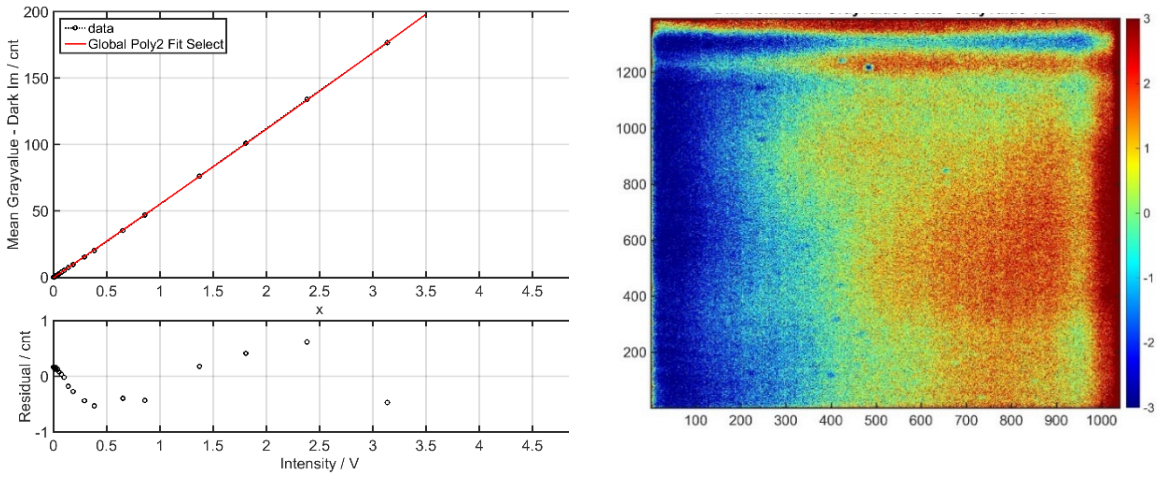

Figure 8: Left: Dependence of the camera output on the intensity. Each point represents the average intensity of 100 images. The red curve is a 2nd order fit to the data points. Right: Deviation of from the averaged image (camera output) at the intensity value of 192 counts.

2.4.1 Spectral sensitivity

Cameras whose sensitivity is optimized for the UV region are rare. Most of the available UV cameras are intended for the use in spectroscopic applications and have therefore a rather large pixel size of 7 µm or more. Such a large pixel size prevents a good approximation of the optical profile in the edge regime, which impedes accurate bidirectional measurements. The CCD camera of the original setup has the micro lens array replaced by a quartz cover glass and exhibits a pixel size of 4.65 µm. Since, by chance, we discovered that the sensitivity of the CMOSIS CMV 4000 chip in the UV regime at 365 nm is about 3 times larger than the sensitivity of the original IPRO CCD camera. It has a micro lens array and exhibits a pixel pitch of 5.5 µm. There remains a certain risk that the UV radiation will damage the chip overtime. However, we did not observe any related disturbances in the images yet. Therefore, the original CCD and a camera based on this CMOS chip is used. Overall, we are still observing the market for a more suitable camera.

2.4.2 Linearity and noise

Both CMOS and CCD cameras show nonlinear deviations in their conversion characteristics. Usually, the detected number of photons is smaller than predicted. While the onset is about 80 % of the saturation of a pixel for CCD cameras it seemed to be about 65 % for CMOS cameras. In addition, the dependence differs slightly from pixel to pixel so that weak patterns appear in the images, which are called fixed pattern noise, even if the camera is illuminated with light of a constant intensity distribution. A schematic of the setup used to determine these deviations is shown in Fig. 7. Here the light of a halogen lamp is homogenized by an Ulbricht sphere and directed towards the camera. The amount of intensity at the camera can be changed by introducing apertures of different diameters in the incoming beam. The intensity change is related to the voltage of a calibrated photo receiver (the monitor diode). Fig. 8 shows the global dependence of the camera output on the intensity (left) and deviation from the mean gray value within the image at the related, fixed intensity level. While the global deviations remain within 1 count, the nonlinear deviations within the field of view vary as much as 6 counts. The same investigations were also performed using a camera with the aforementioned CMOSIS CMV 4000 chip. The size of the intensity deviations was similar but the deviations within the field of view contained more short periodic deviations. The temporal noise behavior of the original CCD camera is documented in Fig. 9. The left diagram shows the global standard deviation as function of intensity. It follows a square root dependence until the intensity approaches the saturation level. The variation of the standard deviation within the camera image is shown on the right side of Fig. 9. It varies by 1.6 counts.

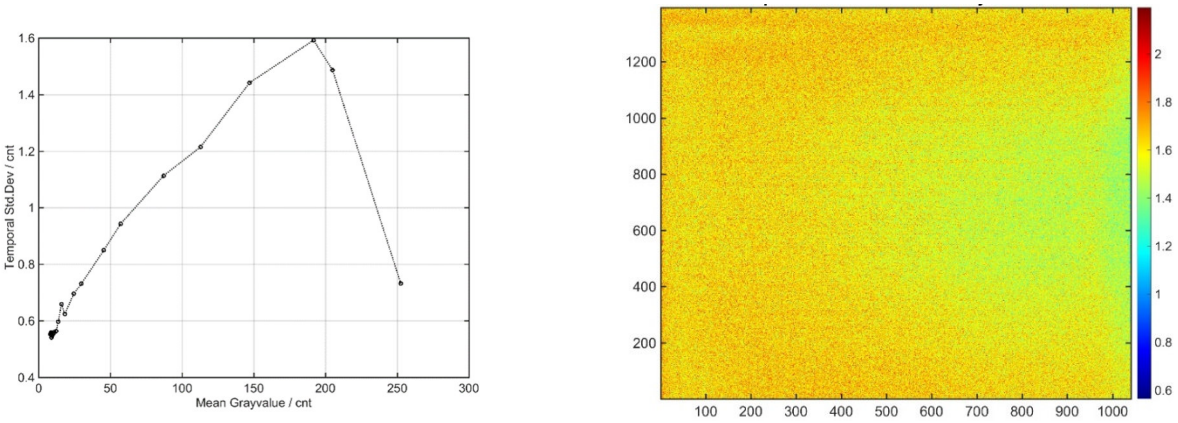

Figure 9: Left: Dependence of the average standard deviation on the intensity. Right: distribution of the standard deviation in the field of view for a mean grey level of 192 counts. In both cases 100 images are used.

The influence of the remaining intensity deviations as well as the temporal noise on the position and on the linewidth of a 1 µm wide line structure was investigated as well. Both values were calculated using a reference intensity profile at different locations within the field of view, which is overlayed by intensity deviations shown in Fig 8 and 9. The line position and width deviations were larger than 1 nm.

If a quadratic correction intensity is determined and applied separately pixel by pixel then the maximum position deviations remained below 0.1 nm. The findings for linewidth deviations are indifferent. Two cameras of the same model were investigated. While the linewidth variations of one camera dropped to about 1.1 nm they remained at 2.3 nm for the other one.

2.4.3 Effective pixel size / deviation of the pixels' positions from the nominal ones

Neither the size of the camera pixel nor the magnification of the microscope is known exactly. For dimensional metrology applications the effective pixel size, that is the size of one pixel in the object space, needs to be calibrated. In principle, there are two different methods. If the lateral motion of the stage is traceably measured, then the position of a suitable structure can be measured at different positions in the field of view using the nominal value of the pixel size. The linear deviations are then used to calculate the effective pixel size. The remaining nonlinear deviations include the deviations of the pixels' positions from their nominal values and the deviations caused by the microscope optics. The latter are denoted as optical distortions. The uncertainty is limited by the repeatability of the structure localization, the remaining nonlinear deviations of the lateral positioning system and by the drift. In the second method a calibrated, 2-dimensional grating is imaged and the position deviations of the features from their nominal positions are used to calculate the effective pixel size and the pixels' position deviations. This is a very fast measurement so that drift influences are eliminated. Here, local deviations of the mean grating pitch represent a hidden source of error. The related influences are usually minimized by averaging calibration data obtained at several different locations of the grating. The results of different comparison of imaging and diffraction methods [6,7] demonstrate that the remaining deviations are sufficiently small if the considered regions on the sample are carefully selected.

The deviations of both calibration methods also include optical distortions. A separation of the distortions introduced by the optics from those of the camera is usually not required. However, here the effective pixel size was calibrated using a 2-dimensional grating. The nonlinear deviations in the center of the field of view remain below 1 nm.

2.4.4 Power consumption and heat dissipation

The power consumption of the camera is especially important because the heat produced by the camera will be guided by the microscope housing into the measurement loops of the instrument. Furthermore, if the camera is located above the measurement object, then the air flux of the air conditioning system will also transport the warmed-up air towards the measurement object. The left side of Fig. 10 shows an image of a CMOS camera mounted on another microscope housing at the test setup acquired using a temperature sensitive infrared camera. During these measurements the camera was operating at an image rate of 25 Hz. The nominal power consumption is specified with 3.6 W. The camera surface heats up to about 35 °C. The diagram on the right side of Fig. 10 shows the temperature drift of the setup when only the measurement camera is turned on. The temperatures changes of the stage, the sample, the objective and the microscope housing and the measurement camera. The latter heat up to about 30.5°C. All other temperatures show only a minor increase, which is in the order of the fluctuations due to the air conditioning system.

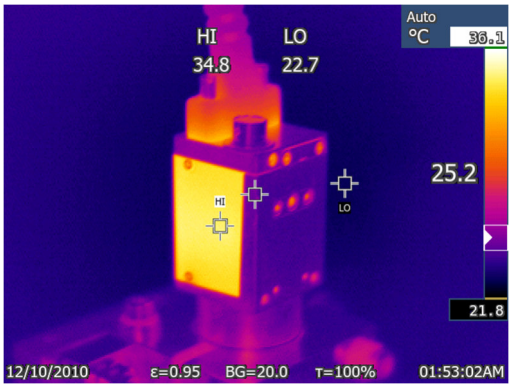

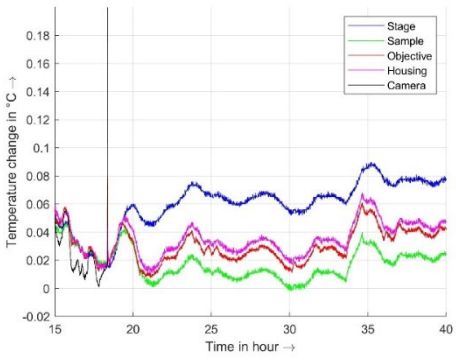

Figure 10: Left: Temperature distribution around a CMOS camera mounted on top of a microscope housing. Right: Temperature change of the test setup caused by turning on the measurement camera.

3. MECHANICAL SETUP

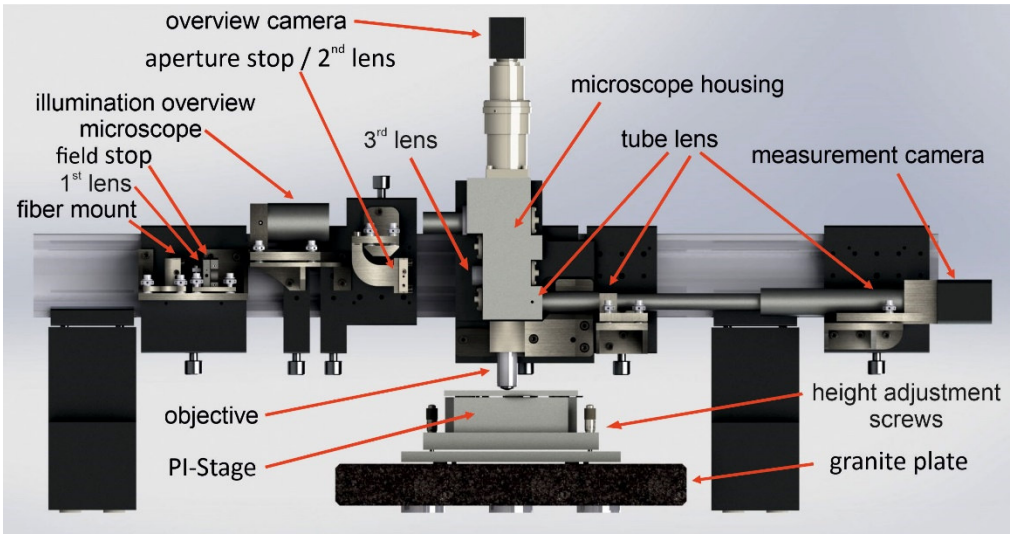

Figure 11: 3D CAD model of the UV microscope mounted at the test setup

The design of the mechanics of the microscope has to address the following tasks:

1. It has to allow to mount the optical elements with the required distance from each other or the sample.
2. It must be possible to align the optical elements to the required specifications while maintaining the required stability / insensitivity against mechanical vibrations and thermal influences.
3. The optics needs to be protected to avoid contaminations and unintentional contacts. In addition, the imaging path needs to be shielded completely so that both refractive index fluctuations and stray light do not lead to instabilities of the image position.
4. The "drive system" has to be able to accept the different measurement objects, provide a mechanism to position the desired structures into the focus plane and into the field of view of the microscope. In addition, the "drive system" need to be able to move with nanometer precision laterally for calibration purposes and with a precision of a few nanometers in vertical direction to acquire image stacks and to focus and to determine the defocus dependencies of the different measurands accurately.

Furthermore, because we want to be able to thoroughly investigate all aspects of optical microscopy for length metrology applications with this setup, the mechanics needs to be sufficiently flexible.

Fig. 11 shows a CAD model of the UV microscope mounted to the test setup. The optical components are attached to a X95 rail system using rail carrier. Only for the microscope housing an additional adapter plate is required that provides the possibilities for a rough lateral, height and angle (in the plane of view) adjustment and serves as spacer to adjust the distance from the X95 system accordingly. The coarse adjustment of the rotation of the microscope housing about the optical axis of the imaging beam path is performed by putting thin metal sheets between the adapter plate and the microscope housing. The fine adjustment of the direction of the illumination and imaging beam is performed by aligning the orientation of the beam splitter and the dichroitic mirror respectively. The objective is mounted on an additional mechanism, which can be aligned separately (see Fig. 12). The whole setup rests on an optical table that provides a passive vibration isolation, and which is located in the clean room center of the PTB. The samples are moved by a specially made 6 axis-controlled flexure stage made by Physik Instrumente (PI). It has a limited motion range of 50 µm x 50 µm x 20 µm. Therefore, the lowest resonance frequency is higher than 400 Hz and the noise level of all axes remain below 1 nm peak to peak. It also provides the z-axis motion required to focus the microscope and for

the acquisition of images at different z-positions (the image stacks of a focus series, or in short focus series). The flexure stage is mounted on a plate containing three micrometer screws that allow a leveling and a coarse positioning of the sample height. This plate rests on three Teflon feet and is located on a granite plate that exhibits a surface flatness of 1 µm. For a lateral coarse positioning the mounting plate containing the flexure stage is moved manually over the granite plate. The dimensions of the granite plate were chosen such that all structures located on a 6" photomask (152 mm x 152 mm x 6,35 mm) can be positioned within the field of view of the microscope. The chosen solution for the coarse approach is simple but allows to position a certain structure on a photomask within a few minutes within the field of view of the microscope if there are either alignment structures or sufficient structures located in the neighborhood. Unfortunately, automatic measurements, for example, of similar structures in different dies on a photomask, are not possible.

The vibrational and thermal sensitivity of the mechanics were optimized using FEM simulations. The results can be summarized as follows:

1. Feet made of solid material influence the thermal and vibrational behavior in a positive way.
2. It is advantageous to locate the right foot in fig. 11 as close as possible to the microscope body.
3. The lowest resonance frequency of the X95 frame is above 100 Hz. It is advantageous to keep the horizontal beam as short as possible and minimize the distance between the 2 feet.
4. Due to the use of the granite plate and the PI-stage, which is made of aluminum, exchanging the X95 frame by a frame made of low expansion material, such as invar, will increase the temperature induced focus drift.
5. If the room temperature varies sinusoidally with an amplitude of 0.1°C and a period of 1 hour then a focus drift of some 10 nm were predicted for the optimized setup.

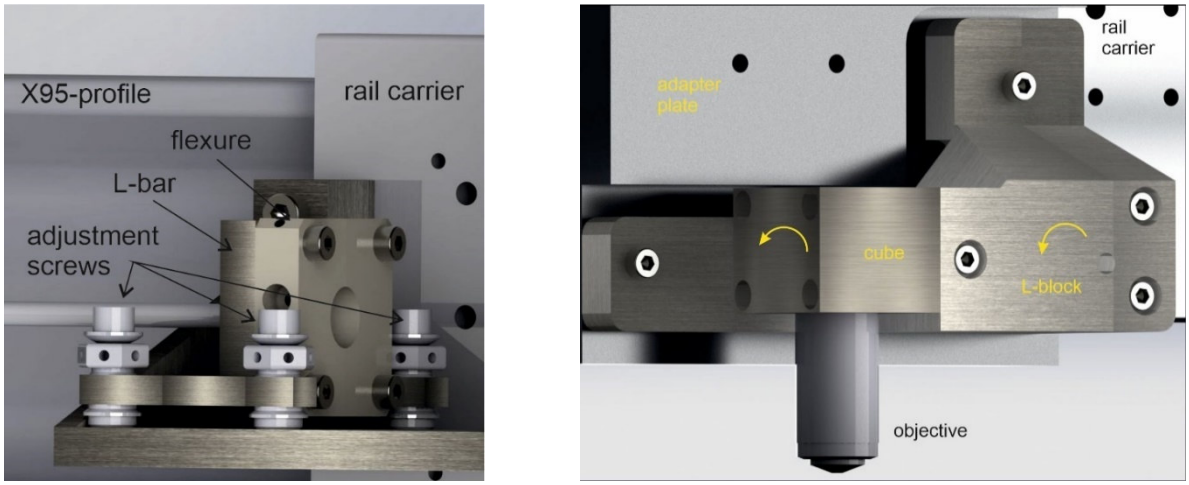

Figure 12: 3D-CAD models of fiber mount for the 365 nm radiation (left) and the objective (right).

The design of all mechanical mounts of the optical elements follows common principles. Therefore, it is sufficient to describe two examples. We like to note here that we do not use kinematic mounts here for two reasons. Firstly, we want to reduce the sensitivity to mechanical vibrations as much as possible. Secondly, it must be avoided that optical elements drop down when they get touched during normal operation by the users unintentionally. We are aware that the setup may therefore be more sensitive to thermal influences.

The left part of Fig. 12 shows the mechanical mount of the optical fiber. It consists of a base plate, which is a L-shaped bar that is mounted to a rail carrier of the X95 system. There is another L-shaped bar connected to the base plate by 3 adjustment screws that carries a 2-dimensional flexure stage [8] in which the fiber is mounted. The bores in the flexure stage are used for coarse adjustment of the lateral direction and the height. The height and the two tilt angles can be adjusted with more sensitivity by the three adjustment screws. The rotation about the z-axis is adjusted by rotating the L-shaped plate using the clearance / tolerances within the bores of the adjustment screws. The flexure stage is used for the final very precise height and lateral adjustment of the fiber.

The mounting of the objective is illustrated in the right part of Fig. 12. On the adapter plate, which is fixed by a rail carrier to the X95-profile, there is a massive L shaped block mounted. To one end of the L-shaped block is a cube screwed that holds the objective. This allows a small rotation around an integrated centering pin within the screw holes to adjust one tilt angle. The massive L-block is used to align the other tilt angle. For this purpose, two height stages are put underneath this block. The fine alignment of the distance between objective and sample is performed by adjusting the height of the mounting plate of the PI-stage using the fine threaded screws (see Fig 11). Adjustment along the direction of the X95 profile is performed by moving the microscope housing (coarse), and the beam splitter and dichroitic mirror respectively. The lateral direction normal to X95 profile does not need to be aligned because the reflective surfaces are larger than the beam diameters. The L-block and the cube may seem to be oversized. But they need to hold an alignment tool (see next section) during the alignment and we may add two mirrors here if we decide to integrate an optical interferometer into the setup (see below).

4. Alignment

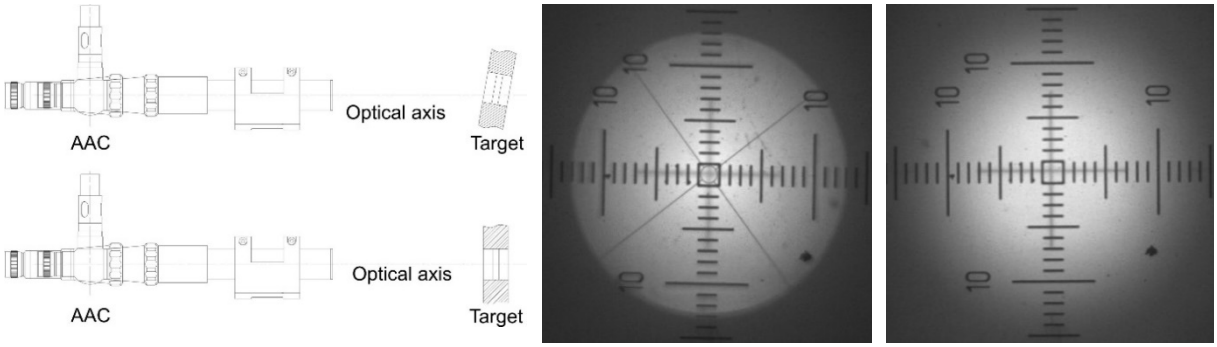

Figure 13: Left: Alignment principle using an alignment autocollimator (AAC) and an alignment target. Middle and right: Images of an alignment target at the end of the alignment, telescope setting (middle) and autocollimator setting (right). The intersection of the crosses without graduation lines shown in the images need to be aligned in the middle of the little square in the center.

The alignment consists of four steps. First the mounting surface of the objective is aligned to be parallel to the surface of the optical table. Next, the optical axis is defined (see below), and the optical elements are aligned to this axis. Then, the lateral position of the aperture stop is aligned so that it is centered and appearing sharp in the back focal plane of the objective using a Bertrand lens. Also, the position of the illumination fiber along the optical axis is adjusted so that its image appears sharp in the back focal plane. Finally, the surface of the measurement object lying on top of the stage is adjusted by an optical probe to be parallel to the surface of the optical table. Assuming that the surfaces are smooth enough and that mounting surfaces of the objective and the alignment autocollimator are normal to the optical axis, the optical axis will also be normal to the sample surface. If the z- axis motion is normal to the top surface of the stage, then the z-axis moves in direction of the optical axis. Because the z-axis of the PI stage has a range of 20 µm only, it is difficult to align it to any axis. However, a misalignment angle between the motion- and the optical axis would lead to a linear defocus dependence of the feature position. However, we observe a quadratic dependence. The remaining misalignment angle thus is in the order of a few mrad only.

The first and the last alignment steps are performed using an optical probe that is moved over the table surface while probing the mounting surface or the sample surface respectively. The orientation of both surfaces is aligned until the probe's reading remain within the noise level.

The optical elements are aligned to the optical axis by means of an alignment autocollimator (AAC) and alignment targets [9]. An AAC is a combination of a telescope and an autocollimator. It contains a movable lens that allows to switch between both functions. The alignment targets (see images in the middle and on the right of Fig. 13) consist of an aligned mirror with a cross in its center. The procedure of this standard alignment principle is outlined in the left schematic of Fig. 13. The target is placed in the optical mount, which is moved and turned until the tilt angles and the lateral position deviations are

small enough. The angles can be aligned to about 0.1 mrad. The accuracy of the position alignment depends on the distance between the AAC and the mount because the magnification of the telescope changes accordingly. In the worst case, at the largest occurring distance, it is about 100 µm. During the whole alignment the AAC is mounted at position of the objective. Its optical axis defines the optical axis of the microscope.

The whole alignment principle is based on the assumptions that the mechanical tolerances of the alignment marks and mounts are sufficiently small and that the optical elements are assembled well centered in their mounts with small tilt angles.

The working distance of the NA=0.9 objective is only 0.3 mm. To avoid any contacts between the sample and the objective the height of sample is prealigned using an optical probe with respect to the height of a stack of gauge blocks. Therefore, directly after the alignment of the whole setup, the PI stage and its mounting plate are removed and the height of the aforementioned stack of gauge blocks is adjusted until the surface of the top one appears sharp in the optical image.

5. DATA ACQUISITION AND EVALUATION

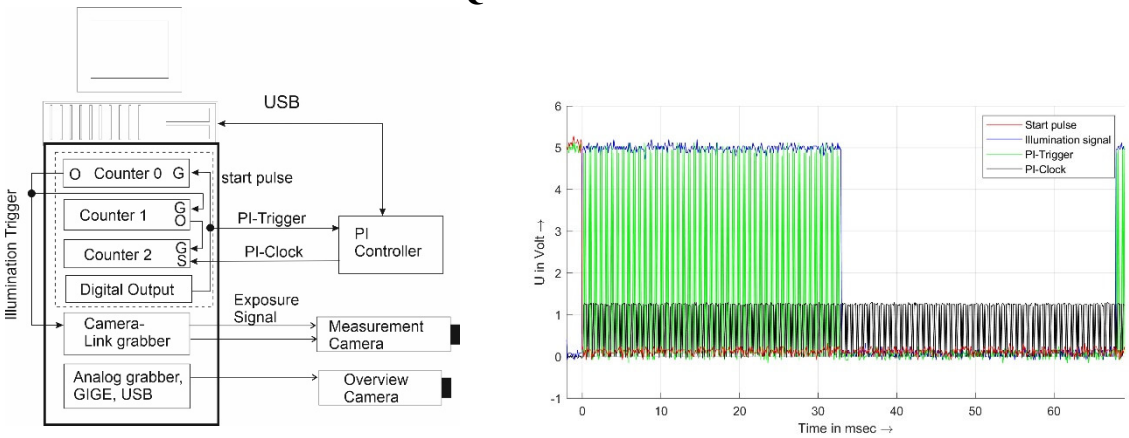

Figure 14: Left: Schematic of the synchronization of the z- axis motion, and the data acquisition of the displacement sensors and the camera. The control computer contains the frame grabbers and an additional counter card. The counter connections are named as O (output), S (source) and G (gate). All timing signals use TTL level and are transferred by BNC cables. Right: Timing signals at the start of an image sequence recorded by an oscilloscope. Note: the amplitude of the PI clock has been reduced in increase the visibility of the other curves.

As already mentioned earlier, the microscope images are acquired by CCD and CMOS cameras using different interfaces. These images need to be displayed, evaluated and saved in the preparation of or during the experiments by the data acquisition program. In addition, to obtain accurate measurements of the feature position the data acquisition of the images and the displacement sensors need to be synchronized with respect to each other and, when image sequences are acquired, to the z-axis motion. Many cameras and displacement sensors do accept external trigger signals so that, by means of providing the camera and the displacements sensors with a common trigger a synchronization can be obtained. Because, usually, the displacement sensor data can be acquired at a much higher rate, it is advantageous to apply a 2nd trigger signal to the displacement sensor that operates close to the maximum trigger frequency and only during the illumination time of the camera. Then the average position value is used for the position of the related image, which reduces the influence of the sensor noise and mechanical vibrations. Depending on the capabilities of the camera, there are two options to obtain the desired synchronization:

1. The illumination of the camera can be controlled by an external trigger pulse (trigger width mode), that is the illumination starts at one edge of the pulse, stops at the other edge, and the pulse duration determines the illumination time. In this case the trigger generator of the camera can gate the trigger generator of the displacement sensors. Another option is to provide both generators with the same time basis and start the trigger generation of both generators at the same time.

2. The camera outputs a pulse during the illumination time, which then can be used to gate the trigger of the displacement sensors.

Using a gate signal may lead to a varying number of position values per image in a series of images, which requires additional efforts in the data acquisition program. Therefore, we use the triggered width mode, provide the trigger generators with the same clock, and start the trigger generation by an additional trigger pulse. At the Nanometer Comparator the triggers are generated by the FPGA card that controls the z-axis motion. In this way the z-axis motion and the trigger generation are synchronized.

Because the motion controller [10] used at the test setup cannot acquire a position reading at a trigger pulse, another apporach had to be implemented. This motion controller allows to start the motion along a trajectory and the recording of its position sensors readings on an external trigger pulse. In addition, it can output a pulse at each point of the motion trajectory. The solution chosen to synchronize these two systems is illustrated in the left part of Fig. 14. A counter card [11] provides and accepts the required timing signals. The source of the three counters is an internal 100 kHz clock. It allows to adjust the illumination signal with a time increment of 10 µsec and to count the pulses of the PI Clock, which exhibit a frequency of 20 kHz. The illumination trigger generated by counter 0 triggers the illumination signal of the frame grabber and gates the output of counter 1. The pulses of counter 1 are applied to the gate of counter 2 that counts the PI clock signal connected to its source, which is set when a position reading is taken by the PI Controller. Through the trigger at its gate the counter 2 saves its value (the number of pulses counted so far) to the internal memory of the counter card. Because the trigger pulses generated by counter 1 are only applied to counter 2 when the camera is illuminated, the numbers of counter 2 are the indices of the position values recorded by the PI controller. To assure that all displacement values are acquired, the output frequency of counter 1 needs to be higher than the frequency of the PI clock. The course of the timing signals at the beginning of a data acquisition sequence are shown in the right part of Fig. 14. Once the image acquisition sequence is finished the position data and the counter values are read and the position values related to an image are determined using the counter value and are averaged. Multiple readings of the same value of counter 2 may occur frequently, which are sorted out before the averaging is performed. The whole data acquisition process is started by a digital pulse, which is also generated by the counter card. It triggers the start of the motion, the generation of the illumination trigger and an event handler function (interrupt handler). This event handler starts counter 2 because its gate is already used to accept a trigger signal. If just images need to be displayed, for example during the alignment process of the sample, then only counter 0 is used.

The implemented approach is very flexible. The brightness of older analog cameras can also be operated conveniently in the trigger width mode using the illumination signal of counter 0. If a camera can just provide an illumination signal, then this is used instead of counter 0 and the illumination signal of the framer grabber.

The user interface of data acquisition program is written in C using LabWindows [12]. Basic data evaluation routines (mean, standard deviation, histogram fit function etc) are taken from the related analysis library. However, the final program is compiled by Microsoft Visual Studio for speed reasons. The data acquisition program also evaluates and shows the defocus behavior of important characteristic parameters like the line position, line width or the edge slope. More detailed analyses are performed using MATLAB. For processing large amount of data mex-files are used, in which the evaluations are performed in parallel by using multiple threads at raised priorities.

6. EXPERIMENTAL RESULTS

6.1 Characterization of the performance of the UV microscope in this setup

The mechanical setup has to provide the ability to characterize the properties of an optical microscope for dimensional metrology applications. Especially, the optical aberrations of the microscope need to be determined accurately. Because the optical aberrations are dependent on the alignment [13] they need to be determined in-situ. A common way is the use of point spread functions (PSF), which includes the accurate imaging and measurement of very small structures below the resolution limit. Because of the strongly reduced contrast here, many images need to be averaged to reduce the intensity noise. Therefore, in the first part of this section, we demonstrate the stability of the measurements. In the second part we then discuss the measurement of the PSF. All investigations discussed here were

performed using the self-assembled LED light source described in section 2.2, an objective with NA of 0.55, the original CCD camera and two different photomasks. An old one is used in the first part and a second, well characterized and high quality one for the determination of the PSF. The design and the characterization of the latter one is provided in [14]. In addition, all mask parameters (optical constants, edge angle, thickness of the different layers, etc) required for the simulation of the optical images have been determined already [14]. To determine the focal position and to eliminate any focus drift influences occurring over the measurement time, no external focus sensor is used. Instead, usually a series of images at different heights (a focus series) are taken from which the exact focus position is determined up in front of any investigation.

6.1.1 Noise and Drift

The two diagrams in Fig. 15 show the course of the line position and the linewidth of cross structure (nominal width of 4 µm) evaluated from 120 images taken consecutively at a data rate of 20 images / sec. The images were taken at the predetermined focus position. For this purpose, a focus series (image stack) containing 20 images at different z-positions in steps of 200 nm is acquired and evaluated within the data acquisition program. The evaluation is restricted to two evaluation windows. Their size and position are selected by the user. One window is evaluated row by row (results are marked by the index x) the other one column by column (index y). The line position and width of each row / column profile

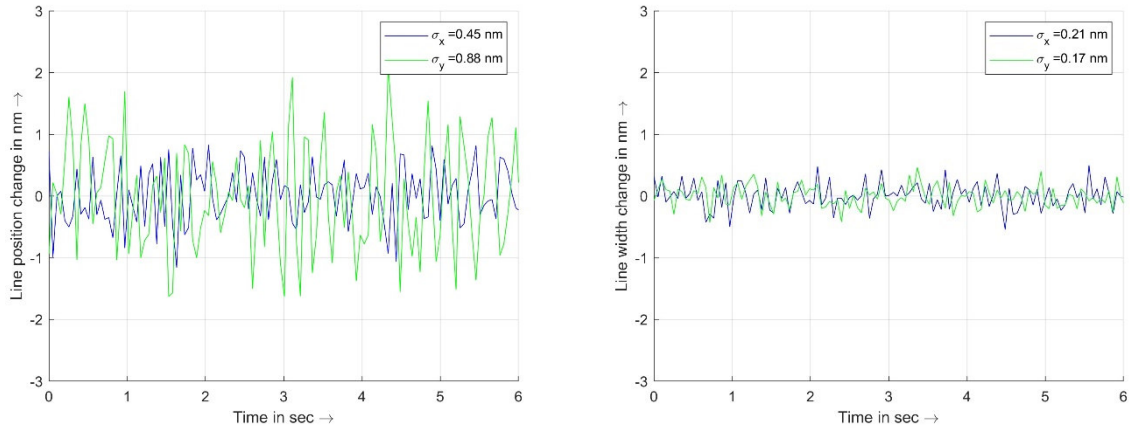

Figure 15: Short term repeatability of the position (left) and the width of a line (right). Further explanations are provided in the text.

are calculated by fitting a polynomial, usually a line, between two predetermined intensity levels of the intensity transition (edge) and interpolating to the position of a fixed intensity level. The sum of both edge positions is the line position and the difference is the linewidth. The line positions / widths of the

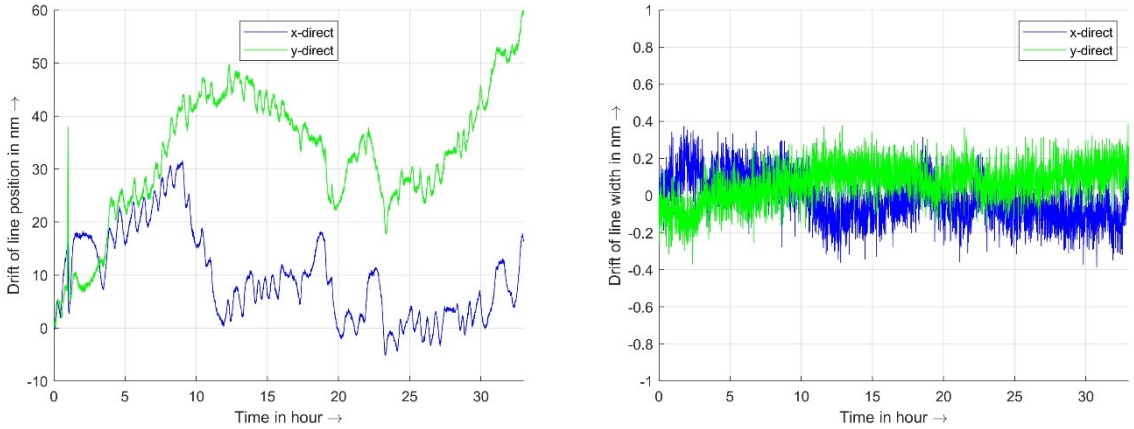

Figure 16: Drift of the line position (left) and the linewidth (right). Each value is calculated for a focus series. The distance in time is about 30 secs. The camera and the illumination of the overview

microscope were turned off and the data acquisition was working for already 12 hours before the measurement was started.

image are the averages of the related values of the evaluation window. The index x refers to the average values of the row wise evaluated window and the index y to the column wise evaluated window. The focus position is determined as z-position of the maximum line edge slope (linear coefficient of the fitting function, also averaged over the evaluation window).

The standard deviations of line position values shown in Fig. 15 are 0.5 nm for the x-direction and 0,9 nm for the y-direction, and those of the line width is about 0.2 nm for both directions. This position noise level is certainly sufficient to investigate structures sizes down to a level of 100 nm, which far below the resolution limit of Rayleigh [15] of 404 nm.

However, with decreasing feature size the contrast reduces as well so that the intensity noise of the camera becomes troublesome. Therefore, for an accurate measurement of the PSF, a lot of more averaging is required. In this case the drift behavior has to be considered. The related curves for the line position and width are provided in Fig. 16. In order to be able to correct the focus drift influence a focus series (41 images, z-distance of 100 nm in-between) were acquired and evaluated. Here, the z - dependence of the line position or width is fitted by a polynomial and the related value at the focus position (maximum slope, as explained above) is used. In comparison to the values shown in Fig. 15 the

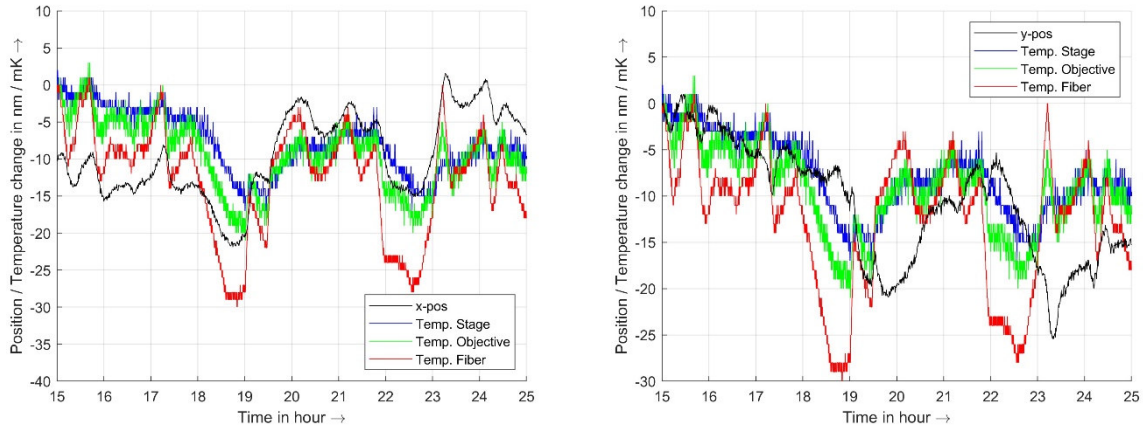

Figure 17: Drift of the line position and the temperature at the flexure stage the objective and the illumination fiber. Note: y-position is shown inverted and set to zero at the beginning of the right diagram.

fitting and interpolation leads to an additional suppression of the noise. While the linewidth variation remains close to the noise level shown in Fig 16, the line position varies by several 10 nm. In these curves there is also a short periodic (about one hour) pattern with an amplitude of a few nanometers due

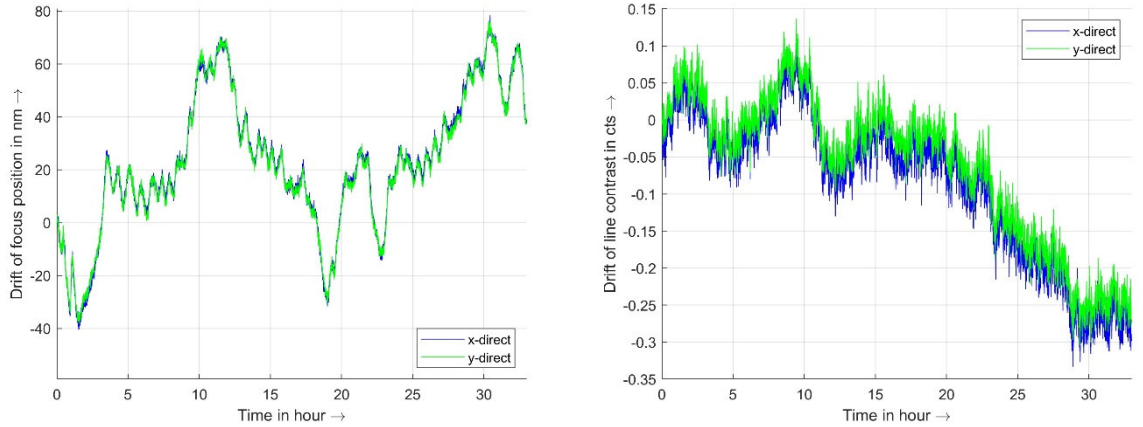

Figure 18: Drift of the focus position (z-position of maximum edge slope, left) and the contrast (averaged over the evaluation window and interpolated to the focus position, right)

to temperature variations of the ambient is visible, which are as shown Fig. 17 in detail. Here drift rates of a below a nanometer to about 15 nm per hour are present. While the lower rate is sufficiently small the higher one may lead to significant influence on the measurement of the PSF. So, the drift in the data needs to be considered.

Additional deviations in the measurement of the PSF may be caused by a strong focus- or contrast drift. The related curves are shown in Fig. 18. While the drift of the contrast is negligible the drift of the focus position needs to be considered as well. Here values up to 30 nm per hour occurred. When a focus drift of more than 20 nm occurs during the measurements the related broadening of the image of the point like object may influence the average image.

6.2 Measurement of the point spread function (PSF)

Because high quality circles with diameters of a few hundred 100 nm and form deviation of a few percent are not available, square-like structures had to be used for the determination of the PSF. The selected photomask has squares down to a side length of 80 nm. An SEM image is provided in the left part of Fig. 19. Based on the visual impression of the signal to noise ratio in the images of the UV microscope, for the further analysis, a square with a nominal side length of 180 nm was selected. The square was moved to the central part of the image. Based on the results of the preceding subsection we decided to acquire 50 focus series with 81 images and a z-distance of 25 nm. So, a z-range of 2 µm around the nominal focus position was covered. Because of the small size of the features and the low contrast / high noise content, the maximum standard deviation [16] was used as focus criterion.

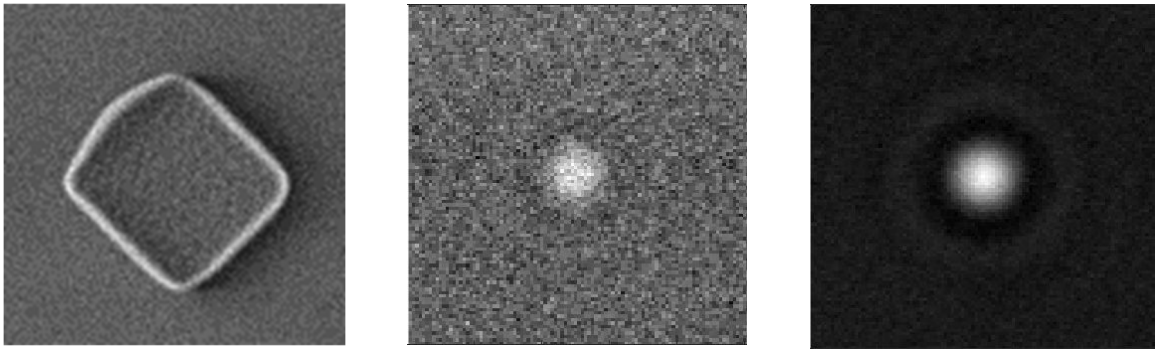

Figure 19: Left: SEM image of a square structure, middle: single image of the UV microscope at focus position (size 2.5 µm x 2.5 µm) and right: averaged focal image.

A 2.5 µm x 2.5 µm wide region of a single image (at focus, flatfield corrected) and the same region averaged over all focal images of the UV microscope are shown in the middle and right part of Fig. 20. At a size of 180 nm the signal to noise ratio improved so far that the drift of the lateral and focus position could be determined. For this purpose, a Gaussian function was fitted to the focal images and the peak

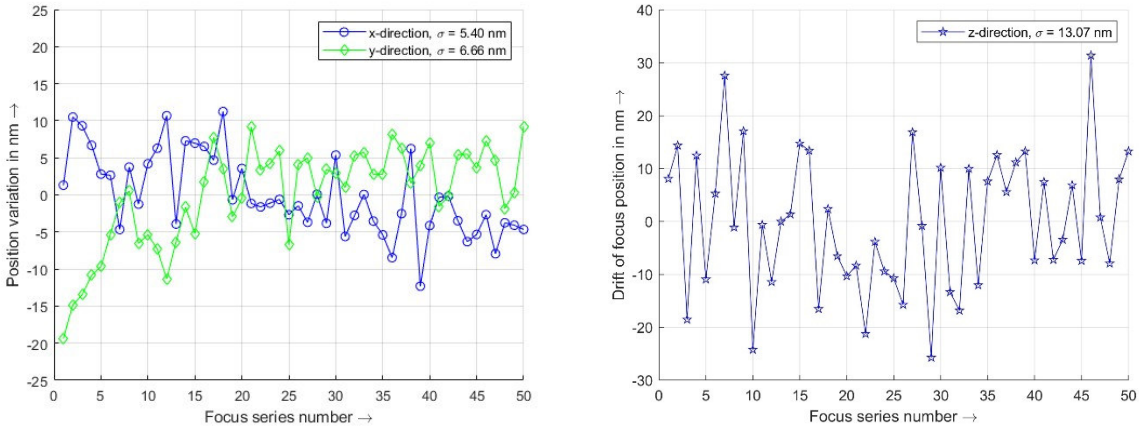

Figure 20: Drift of the lateral (left) and the focus position (right) during the data acquisition

positions were used as position indicators. The related curves are shown in the left diagram of Fig. 20. It seemed that a small drift in the y-direction of about 15 nm, which is less than the size of 1 pixel occurred over the first five focus series. The x-direction and the focus position show no drift at all. In a first step of the data analysis an Airy disc was fitted to the averaged focal image (right part of Fig. 19) using a nonlinear least-squares fit in MATLAB. The fitted Airy disc is given by

$$S = K_1 \left[\frac{J_1\left(2\pi\, NA\frac{r}{\lambda}\right)}{2\pi NA\frac{r}{\lambda}} \right]^2 + K_0 \qquad (1)$$

where S denotes the optical power, J_1 the 1st order Bessel function of the 1st kind, λ the wavelength, NA the numerical aperture of the objective and r the distance from the center position of the peak. The wavelength λ was measured by a spectrometer and the numerical aperture NA was determined using the method described in [17] before. Fitted were the constants K_1, K_0 and the center coordinates (x_0, y_0), which are used to calculate r according to

$$r = \sqrt{(x - x_0)^2 + (y - y_0)^2} \qquad (2)$$

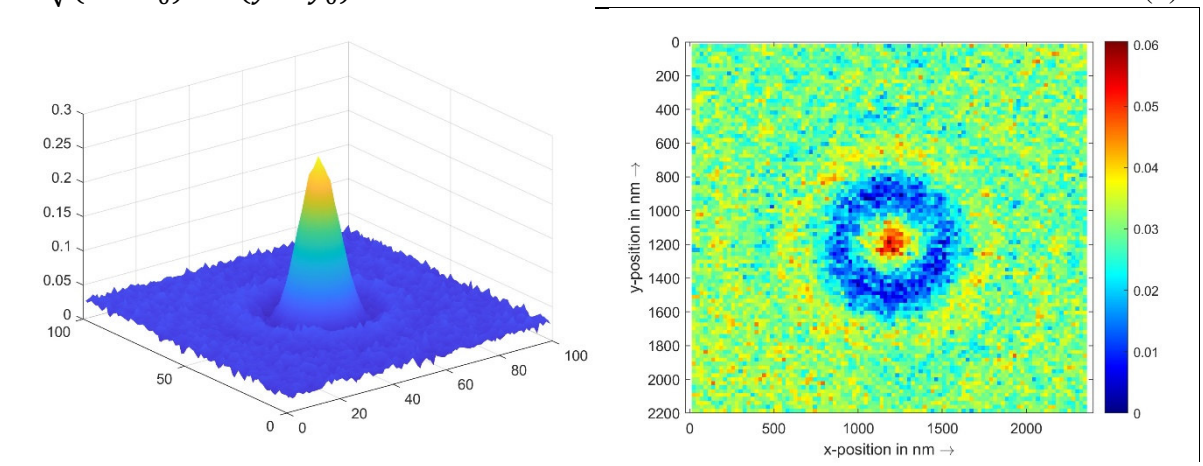

Figure 21: 3D representation of the measured PSF (left) and the residuals of nonlinear fit of the Airy disc to according Eqs. (1) and (2). Note: In both images the minimum value was subtracted to ease the recognition of the maximum values.

The left diagram of Fig. 22 shows a 3D representation of the measured PSF. The maximum value is about 0.15. The fit residuals of the Airy disc fit are provided in the right diagram. There are some ring-like structures left, which are caused by the remaining optical aberrations. The residuals are highly rotational symmetric. Therefore, angle dependent aberrations like Coma or Astigmatism are not present.

In the further analysis we follow the approach of Nijboer [18]. According to the results of the scalar diffraction theory the PSF of an aberrated system at a defocused image plane can be calculated by

$$U(r, \varphi, f) = \frac{1}{\pi} \iint exp\,(if\rho^2) P(\rho, \vartheta) exp[2\pi i \rho r\, cos(\varphi - \vartheta)] \rho d\rho d\varphi \qquad (3)$$

Here U denotes the electric field. The first e-function term describes the amount of defocus, the second the diffraction of a spherical wave and P is the pupil function, which contains the aberrations. R, φ and ρ, ϑ are the cylindrical coordinates in the image plane at f = -i2πz and in the exit pupil. The pupil function P has the form

$$P(\rho, \vartheta) = A(\rho, \vartheta)\, \exp[i\Phi(\rho, \vartheta)], \qquad (4)$$

where A describes the transmission, which is set to one, and Φ represents the wavefront aberrations. The latter are usual described using Zernike polynomials [19]. That is

$$\Phi(\rho,\vartheta) = \sum_{n,m} C_n^m R_n^m(\rho)[\sin(m\vartheta) + \cos(m\vartheta)], \tag{5}$$

where $R_n^m(\rho)$ are given by

$$R_n^m(\rho) = \sum_{l=0}^{\frac{n-m}{2}} \frac{(-1)^l (n-l)!}{l!\left(\frac{1}{2}(n+m)-l\right)!\left(\frac{1}{2}(n-m)-l\right)!} \rho^{n-2l} \tag{6}$$

The analytical solution of eq. (3) in the focal plane is then [18]

$$U(r,\varphi) = 2\sum_{n,m} i^m (-1)^{\left(\frac{m-n}{2}\right)} C_n^m \frac{J_{n+1}(2\pi NA\, r/\lambda)}{2\pi r\, NA/\lambda} \cos(m\varphi). \tag{7}$$

Therefore, through a fit of Eq. (7) to the experimentally obtained PSF shown in Fig.21, the Zernike coefficients C_n^m of the wavefront aberrations Φ of Eq. (5) and thus the pupil function P of Eq. (4) can be determined. The pupil function has to be included in the calculation / simulation of the optical images

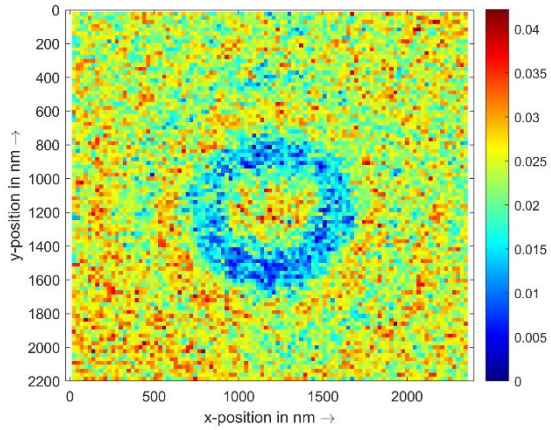

Figure 22: Residuals of the fit of the aberrated PSF Eq. (7) to the experimentally obtained data shown in the left part of Fig. 21.

to account for the influence of the optical aberrations, which is required in the evaluation of bidirectional optical measurements. Therefore, the determination of the optical aberrations can be considered as the final step of a calibration of an optical microscope or vision based dimensional metrology system.

As already mentioned above, in the data considered here, there are no angle dependent aberrations present. We like to note, that the Bessel functions in Eq. (7) are not orthogonal over the unit circle. Consequently, all terms in the sum in Eq. (7) have to be fitted in one step. The residuals of such a fit just containing the first two radial symmetric terms (defocus and spherical aberrations) are shown in Fig. 22. The size of the residuals reduced by about 30%. But there is still a ring like structure present, which is in order of the noise level. Including higher order terms did not lead to a further reduction of the residuals.

7. SUMMARY AND OUTLOOK

In this paper, we described a microscope test setup, which has been optimized using FEM calculations, and the integration of a high-performance UV microscope in this setup. In addition, we discussed the influence the main components, such as the light source or the camera, on the performance of the microscope and provided related data. Then, we also explained schematically the alignment procedure. Furthermore, we developed a hardware concept that allows to acquire the image and position data as synchronously as possible, is flexible enough to integrate different cameras and allows to experiment with different data acquisition schemes. In the last section, we proofed experimentally that this setup allows a complete characterization of high-resolution microscope including the measurement of a PSF.

The results of these measurements demonstrate the high quality of the alignment and the microscope optics. However, the quantitative analysis of the PSF is not complete yet and the related results cannot be compared to the more elaborated approaches referred to below. However, the drift influences of the lateral position need to be observed and may, from time to time, become too large. Therefore, the integration of an optical interferometer measuring the position change between the microscope objective and the granite plate differentially seems to be advisable. This would, very likely, also reduce the influence of mechanical vibrations even further. We like to mention here, that there seemed to be no detailed investigation of the influence of motion blur on the measurement of the PSF published so far. Our findings documented in [20,21] indicate that there remains still an influence.

The Zernike Nijboer theory is based on scalar diffraction. The limitations of this theory have already been observed in optical linewidth measurements [22]. In parallel, in collaboration with others, we pursue the development of a simulation-based approach to determine the optical aberrations [23,24]. These far more complex treatments are beyond the scope of this paper.

In the near future, we will also include the high numerical aperture objectives in the experimental investigations. So far, we are only able to use unpolarized light. However, in [25, 26], it has been demonstrated that the polarization of the light has a significant influence on linewidth measurements. Currently, an illumination optics that will allow to adjust the polarization angle of the incoming light continuously is under development. The challenge here is to integrate the rotation of the polarizer in such a way that illumination of the sample is not influenced otherwise.

ACKNOWLEDGEMENTS

The authors like to thank W. Haessler-Grohne (PTB) for numerous discussions on the experimental issues, E. Buhr (PTB) providing input related to optical microscopy and J. de Vries (IBS Precision Engineering. Eindhoven, Netherlands) for the discussion of optical design issues. This project is funded by the German Federal Ministry of Education and Research (BMBF, project number 01IS20080B, SiM4diM).

REFERENCES

[1] R. Köning, C.Weichert, B. Przebierala, J. Flügge,W. Haessler-Grohne and H. Bosse, “Implementing registration measurements on photomasks at the Nanometer Comparator”, Measurement Science and Technology, IOP Publishing , Bristol, United Kingdom, 094010 (9pp), **23** (2012).

[2] G. Schlueter, K.-D. Roeth, C. Blaesing-Bangert, M. Ferber,“ Next generation mask metrology tool“, Photomask and Next-Generation Lithography Mask Technology IX, Proceedings of SPIE Vol. **4754**, 758 - 768 (2002). Remark: The reference describes the design of the LMS IPRO 2. The IPRO 4 uses the same interferometers and the same microscope but has a smaller motion range and improved software. There is no reference of the IPRO 4 that provides more than measurement results that indicate the performance, documented, for example, in
C. Enkrich, G. Antesberger, O. Loeffler, K.-D. Roeth, F. Laske, K.-H. Schmidt, D. Adam, “Registration measurement capability of VISTEC LMS IPRO4 with focus on small features”, Photomask and Next-Generation Lithography Mask Technology XV, Proceedings of SPIE Vol. **70282**, 70282Y (2008),

[3] J. Krüger, R.Köning, B. Bodermann,“ Characterization progress of a UV-microscope recently implemented at the PTB Nanometer Comparator for uni- and bidirectional measurements“, Proc. EOSAM 2020, E PJ Web of Conferences **238**, 06010 (2020) . open access, available at https://doi.org/10.1051/epjconf/202023806010

[4] M365D2 LED with ITC 133 Controller, Thorlabs equipped with a low noise, linear power supply.

[5] E. Buhr, M. Schulz: „Determination of Imaging Properties of CCD Still Cameras - ISO Standards and Measuring Facilities at the Physikalisch-Technische Bundesanstalt“, 3rd International Symposium on Electronic Photography (ISEP’96), Köln, 21 – 22 September 1996, in: IS&T Proceedings of The Third International Symposium on Electronic Photography (ISEP ‘96). F. Granzer, J.C. Owens (Eds.), IS&T-The Society for Imaging Science and Technology, Springfield, Virginia, USA, 26-31 (1996)

[6] E. Buhr, W. Michaelis, A. Diener and W. Mirande ,“Multi-wavelength VIS/UV optical diffractometer for high-accuracy calibration of nano-scale pitch standards“, Measurements Science and Technology, IOP Publishing , Bristol, United Kingdom, 667- 674, **18** (2007)

[7] J.-A. Kim, J. W. Kim, B. C. Park and T. B. Eom, “Measurement of microscope calibration standards in nanometrology using a metrological atomic force microscope”, Meas. Sci. Technol. IOP Publishing , Bristol, United Kingdom **,** 1792–1800,**17**, (2006)

[8] fle.X-plate, 2D-flexure stage with 0.5 mm range, QIOPTIQ, Göttingen, Germany

[9] This method seems to a be standard procedure in the optics industry. They alignment or focusing autocollimators are available from Moeller-Wedel Optical or TRIOPTICS.
[10] Digital Controller E-712, Physik Instrumente, Kalsruhe, Germany
[11] Multipurpose Counter card, for example model 6601/2 or 6612 of National Instruments, USA
[12] LabWindows / CVI, C Development Environment, National Instruments, USA
[13] J. Schwiegerling, "Review of Zernike polynomials and their use in describing the impact of misalignment in optical systems", Conference on Optical System Alignment, Tolerancing, and Verification XI, Proc. SPIE ,103770D, Vol. **10377** (2017)
[14] W. Mirande, B. Bodermann, W. Haessler-Grohne, C. G. Frase, S. Czerkas and H. Bosse, "Characterization of new CD photomask standards", Proceedings of Metrology, Inspection, and ProcessControl for Microlithography XVIII, SPIE 29-40, **5375** (2004); doi: 10.1117/12.533734
[15] X. C. de Lega and P.J. de Groot, "Lateral resolution and the instrument transfer function as criteria for selecting surface metrology instruments", in *Imaging and Applied Optics Technical Papers*, OSA Technical Digest (online) Optica Publishing Group, paper OTu1D.4, DOI: 10.1364/OFT.2012.OTu1D.4 (2012)
[16] Y.Sun, S. Duthaler, AND B. J. Nelson," Autofocusing in Computer Microscopy: Selecting the Optimal Focus Algorithm", Microscopy Research and Technique, J. Wiley & Sons, Hoboken, USA, 139-149, **65**, 2004
[17] J. Krüger, D. Bergmann, R. Köning, B. Bodermann and E. Manske, „In situ, back-focal-plane-based determination of the numerical apertures in optical microscopes", Applied Optics, OPTICA PUBLSIHING GROUP, Washington, USA, 756-763, **62** (2023)
[18] J. J.M. Braat, P. Dirksen, S. van Haver, A. J.E.M. Janssen, "Detailed description of the ENZ approach", available at NijboerZernike.nl - Extended Nijboer Zernike Analysis (ENZ), last accessed at 26.6.2023.
[19] V. Lakshminarayanan and A. Fleck,"Zernike polynomials: a guide", Journal of Modern Optics, Taylor & Francis, London,UK ,545-561, **58** (2011)
[20] J: Krüger, B. Bodermann, R. Köning, P. Manley, L. Zschiedrich, P.-I Schneider, A. Heinrich, C. Eder, A. Goehnermeier," On Aberration Retrieval for optical Microscopes in length Metrology", to be published in the conference proceedings of Modeling Aspects in Optical Metrology, part of the SPIE meeting on Optical Metrology held in Munich, Germany from June 23th to 26th.
[21] J: Krüger, B. Bodermann, R. Köning, P. Manley, L. Zschiedrich, P.-I Schneider, "Untersuchung des Schwingungseinflusses auf gemessene Punktspreizfunktionen in der optischen Mikroskopie",proceedings of the DGAO Tagung, 2022, online available at DGaO Proceeding (dgao-proceedings.de), in German
[22] M. Czaske: Strukturbreitenmessung auf photolithographischen Masken und Wafern im Licht-mikroskop: Theorie, Einfluß der Polarisation des Lichtes und Abbildung von Strukturen im Bereich der Auflösungsgrenze, PTB-Opt-**55**, PhD thesis, Braunschweig (1997), ISBN 3-89701-011-9
[23] P.-I. Schneider, P. Manley, J. Krüger, L. Zschiedrich, R. Köning, B.Bodermann, S. Burger, "Reconstructing phase aberrations for high-precision dimensional microscopy", Proc. SPIE 12137, Optics and Photonics for Advanced Dimensional Metrology II, 121370I, SPIE Photonics Europe 2022, Strasbourg, France
[24] J. Krüger, R.Köning, B. Bodermann, "A phase retrieval inspired approach for the determination of optical aberrations in microscopy", Euspen - 1st Virtual International Conference (originally: euspen - 20th International Conference and Exhibition, Geneva, Switzerland), Virtual Conference, 8-12, June, 2020,
[25] M. Totzeck: "Numerical simulation of high-NA quantitative polarisation microscopy and corresponding near-fields", Optik **112** (2001), 399-406
[26] B. Bodermann, G. Ehret, W. Mirandé: "UV and DUV microscopy for dimensional metrology on micro- and nano-structures", Proc. SPIE **5457**, (2004), 35 - 43

CONTACTS

Dr.-Ing. R.Köning

email: rainer.koening@ptb.de
ORCID: https://orcid.org/0000-0003-2706-7013